

Inverse Problems for Inertial Sensor Calibration

David L. Olson

May 11, 2025

Contents

| | | |
|----------|--|-----------|
| 1 | Introduction | 3 |
| 1.1 | Defining Sensor Error | 3 |
| 1.1.1 | Basic IMU Error Sources and Error Models | 4 |
| 1.1.2 | Traditional Inertial Sensor Calibration | 5 |
| 1.2 | Beyond Traditional IMU Calibration | 6 |
| 2 | Methods | 7 |
| 2.1 | STIM 300 IMU Specifications | 7 |
| 2.2 | Simulating Calibration Data and Model Parameters | 7 |
| 2.3 | Formulating IMU Calibration as a Discrete Linear Inverse Problem | 8 |
| 2.4 | Assessing Singular Values | 10 |
| 2.5 | L2 Regression without a Known Normal Distribution | 10 |
| 2.6 | Motion Profile Evaluation | 11 |
| 3 | Results | 14 |
| 3.1 | Traditional Calibration Sequence | 14 |
| 3.2 | New Motion Profile Evaluation | 15 |
| 3.2.1 | Motion Profile 1: Single-Axis Tilts in One Direction | 15 |
| 3.2.2 | Motion Profile 2: Single-Axis Tilts in Both Directions | 18 |
| 3.2.3 | Motion Profile 3: Multi-Axis Tilts in All Directions | 21 |
| 3.3 | IMU Calibration for Ill-Conditioned System Dynamics | 24 |
| 4 | Discussion | 28 |
| 4.1 | A Comparison to the Traditional Means of Calibration | 28 |
| 4.2 | A Comparison of the Three Motion Profiles | 28 |
| 4.3 | IMU Calibration for Ill-Conditioned System Dynamics | 30 |
| 5 | Conclusion | 32 |
| 6 | Appendix | 35 |
| 6.1 | Traditional IMU Calibration Post-Processing | 35 |

Abstract

Inertial sensors are vital to navigation, guidance, and control for a variety of vehicles such as self-driving cars. Inertial sensors, i.e., accelerometers and gyroscopes, measure specific and angular velocity respectively. These measurements are propagated to produce a position, velocity, and attitude solution for the vehicle, all three of which are necessary for proper vehicle navigation. Like any other sensor, all inertial sensors are subject to both deterministic and stochastic error which require careful calibration and characterization before use in any vehicle. In industry, the current state of the art for inertial sensor calibration has made little advancement over the past couple decades. Traditionally, hours of high-rate inertial sensor data is collected in static poses or constant angular rates and post-processed in piecemeal sections which average over these long periods of collected data to compute basic error model parameters. These traditional methods provide no ability to assess any uncertainty in the computed parameters, making any judgments about the fidelity of the calibration subjective. Regardless, instead of investigating advanced algorithms for estimating calibration parameters, industry achieved for high-fidelity calibrations solely via purchasing higher and higher precision equipment, which eventually succumbs to the law of diminishing returns.

However, ongoing academic research addressing inertial sensor calibration seeks to break dependence on high-cost high-precision test equipment by introducing advanced estimation techniques, often referred to as systematic calibration. While various papers only tackle small pieces of an entire calibration procedure, there is an opportunity to cast inertial sensor calibration as an inverse problem to provide a holistic methodology to the field. The forward problem is the transformation of true dynamic inputs acting on the sensor into sensor outputs which are subject to error. Then, the inverse problem takes the form of calibration in which the model parameters are estimated from collected sensor data. Using inverse problem techniques, calibration parameter estimation can advance beyond these piecemeal strategies to achieve a higher-fidelity solution as well as provide metrics to assess the uncertainty and correlation between model calibration parameters.

This work focused on posing inertial sensor calibration as an inverse problem which included modeling inertial sensor error and rotational test bed dynamics. This provided an opportunity to employ linear inverse problem techniques, even in the presence of ill-conditioned model operators caused by the modeled table dynamics. In addition, the model covariance and correlation between parameters was also analyzed, which is rarely reported in any academic literature. In summary, this work highlighted both the benefits and additional considerations needed for systematic calibration.

1 Introduction

A key challenge for self-driving cars is autonomous navigation. Common sensors for self-driving car navigation include inertial measurement units (IMUs), global positioning system (GPS) receivers, odometers, magnetometers, radars, LiDAR, cameras, and many others. Autonomous navigation fuses the inputs of multiple sensors to formulate a position, velocity, and attitude (PVA) solution for the vehicle of interest. It is crucial to not only formulate a navigation solution but also to track the uncertainty of that solution, which can play an important role in decision-making and risk-assessment for autonomous self-driving vehicle autonomous operation.

IMUs generally contain three accelerometers and gyroscopes pointing in all three Cartesian axes which measure specific force and angular velocity respectively. These measurements are integrated to provide a PVA solution, but an IMU-only solution will drift away from truth unbounded due to the integration of sensor noise and other errors [1]. An inertial navigation system (INS) integrates the IMU measurements and then uses GPS to provide accurate measurements of position to fuse with the IMU solution typically via a Kalman filter thus combating any position error drift. This allows for long-term accurate navigation suitable for a self-driving car traveling long distances.

A driving need for navigation regarding self-driving cars is forming back-up modes of navigation when GPS signals are temporarily unavailable. This is especially important in urban environments where tall buildings and tunnels can cause signal blockages. Lack of GPS signals are problematic for an INS as its performance is dependent on receiving those signals, and the IMU-only solutions will drift away quickly from ground truth. Inertial-only navigation is suitable for short periods such as temporary GPS signal blockages, but the duration of a suitable inertial-only navigation is highly dependent on the quality of sensors contained within an IMU. This dilemma, among any others, motivates the need for rigorous IMU calibration and compensation.

1.1 Defining Sensor Error

Accelerometers and gyroscopes are subject to a variety of error sources such as biases, scale factor imperfections, axis misalignments, noise, and many others. IMU *calibration* is the process of characterizing these error sources, while *compensation* is the process of correcting measurements in real-time to provide the most accurate and precise measurements possible. The better these error sources are characterized, the slower that the IMU-only navigation solution will drift away from truth.

Inertial sensor calibration can be treated as an inverse problem. Consider an accelerometer as an example where the ideal forward model is quite straight forward; specific force in equals specific force out. Unfortunately in practice, we are not quite so lucky. Any error in the forward model is defined as

$$\Delta f := \tilde{f} - f$$

where Δf is the measurement error, \tilde{f} is the specific force measured by the sensor which is subject to error, and f is the true specific force acting on the accelerometer. The same applies to gyroscope measurements.

$$\Delta\omega := \tilde{\omega} - \omega$$

Inertial sensor errors Δf and $\Delta\omega$ are subject to both deterministic and stochastic error and any number of contributing factors can make up these terms.

There are many procedures available to calibrate inertial sensors such as [2] which require high-precision equipment to point and spin inertial sensors at known directions or quantities to separate measurement truth from measurement error.

1.1.1 Basic IMU Error Sources and Error Models

Consider an IMU which contains three accelerometers and three gyroscopes arranged to point in a standard Cartesian right-handed coordinate frame. A basic forward model framework appropriate for commercial- and automotive-grade inertial sensors is provided in [1].

$$\begin{aligned}\tilde{\mathbf{f}} &= [I + M_a] \mathbf{f} + \mathbf{b}_a + \mathbf{w}_a, \quad \mathbf{w}_a \sim N(0, \sigma^2) \\ \tilde{\boldsymbol{\omega}} &= [I + M_g] \boldsymbol{\omega} + \mathbf{b}_g + \mathbf{w}_g, \quad \mathbf{w}_g \sim N(0, \sigma^2)\end{aligned}\tag{1}$$

In these models are bias terms $\mathbf{b}_a, \mathbf{b}_g \in \mathbb{R}^3$ for the accelerometers and gyroscopes respectively. In addition are the misalignment matrices $M_a, M_g \in \mathbb{R}^{3 \times 3}$, whose diagonal elements are scale factor error terms. The off-diagonal elements are misalignment terms which account for imperfections in the alignment of the sensing axes. All inertial sensors are also subject to noise, which is captured by terms $\mathbf{w}_a, \mathbf{w}_g$ which are additive zero-mean white Gaussian noise. Equation 2 restates equation 1 in terms of all its various elements.

$$\begin{aligned}\begin{bmatrix} \tilde{f}_x \\ \tilde{f}_y \\ \tilde{f}_z \end{bmatrix} &= \begin{bmatrix} 1 + s_{a,x} & m_{a,xy} & m_{a,xz} \\ m_{a,yx} & 1 + s_{a,y} & m_{a,yz} \\ m_{a,zx} & m_{a,zy} & 1 + s_{a,z} \end{bmatrix} \begin{bmatrix} f_x \\ f_y \\ f_z \end{bmatrix} + \begin{bmatrix} b_{a,x} \\ b_{a,y} \\ b_{a,z} \end{bmatrix} + \begin{bmatrix} w_{a,x} \\ w_{a,y} \\ w_{a,z} \end{bmatrix} \\ \begin{bmatrix} \tilde{\omega}_x \\ \tilde{\omega}_y \\ \tilde{\omega}_z \end{bmatrix} &= \begin{bmatrix} 1 + s_{g,x} & m_{g,xy} & m_{g,xz} \\ m_{g,yx} & 1 + s_{g,y} & m_{g,yz} \\ m_{g,zx} & m_{g,zy} & 1 + s_{g,z} \end{bmatrix} \begin{bmatrix} \omega_x \\ \omega_y \\ \omega_z \end{bmatrix} + \begin{bmatrix} b_{g,x} \\ b_{g,y} \\ b_{g,z} \end{bmatrix} + \begin{bmatrix} w_{g,x} \\ w_{g,y} \\ w_{g,z} \end{bmatrix}\end{aligned}\tag{2}$$

The goal of IMU calibration is characterize to these IMU error sources, resulting in estimates $\hat{\mathbf{b}}_a, \hat{M}_a, \hat{\mathbf{b}}_g, \hat{M}_g$ which then allows for the correction of inertial sensor measurements in real-time, which is referred to as compensation. In essence, this can be treated as the inverse model with estimated parameters. Using the estimated model parameters, inertial sensor measurements $\tilde{\mathbf{f}}, \tilde{\boldsymbol{\omega}}$ are compensated to provide new measurements $\hat{\mathbf{f}}, \hat{\boldsymbol{\omega}}$ per equation 3.

$$\begin{aligned}\hat{\mathbf{f}} &= [I + \hat{M}_a]^{-1} (\tilde{\mathbf{f}} - \hat{\mathbf{b}}_a) \\ \hat{\boldsymbol{\omega}} &= [I + \hat{M}_g]^{-1} (\tilde{\boldsymbol{\omega}} - \hat{\mathbf{b}}_g)\end{aligned}\tag{3}$$

Equation 2 does not contain an exhaustive list of potential error model parameters. The IEEE standards [3, 4, 5, 6, 7, 8, 9] contain detailed model for an individual inertial sensor, but not a

full-fledged IMU. These standards are summarized in [10], however some model parameters may be important than others depending on the technology of the inertial sensor in use.

1.1.2 Traditional Inertial Sensor Calibration

IMUs are calibrated on some sort of a rotational test bed. These rotation test beds are able to point and spin inertial sensors at known quantities with sharp precision. To calibrate accelerometers, the IMU is aligned in various poses along the local gravity vector at that location, therefore a gravity survey within an inertial test laboratory is critical. To calibrate gyroscopes, the IMU is spun at known speeds.

For example hardware, consider the 2103C Series Three-Axis Position and Rate Table System from Ideal Aerosmith [11] shown in figure 1.



Figure 1: 2103C Series Three Axis Position and Rate Table System

Traditional calibration comprises of twelve tests with six for the accelerometers and six for the gyroscopes. In each test, the IMU is stationary for accelerometer tests and spinning at a constant speed for gyroscope tests. Each test is completed for a set amount of time, usually 60 seconds, and the measurements are averaged. Table 1 lists the six tests as well as the quantity for each averaged test result.

| Accelerometer Tests | Gyroscope Tests |
|--|--|
| <ul style="list-style-type: none"> • Point X-Axis Up ($\bar{\mathbf{f}}^{+x}$) • Point X-Axis Down ($\bar{\mathbf{f}}^{-x}$) • Point Y-Axis Up ($\bar{\mathbf{f}}^{+y}$) • Point Y-Axis Down ($\bar{\mathbf{f}}^{-y}$) • Point Z-Axis Up ($\bar{\mathbf{f}}^{+z}$) • Point Z-Axis Down ($\bar{\mathbf{f}}^{-z}$) | <ul style="list-style-type: none"> • Positive Spin about X-Axis ($\bar{\omega}^{+x}$) • Negative Spin about X-Axis ($\bar{\omega}^{-x}$) • Positive Spin about Y-Axis ($\bar{\omega}^{+y}$) • Negative Spin about Y-Axis ($\bar{\omega}^{-y}$) • Positive Spin about Z-Axis ($\bar{\omega}^{+z}$) • Negative Spin about Z-Axis ($\bar{\omega}^{-z}$) |

Table 1: Traditional IMU Calibration Tests

As an example from equation 2, the accelerometer bias \mathbf{b}_a can be solved from the collected test data.

$$\mathbf{b}_a = \begin{bmatrix} b_{a,x} \\ b_{a,y} \\ b_{a,z} \end{bmatrix} = \frac{1}{2} \begin{bmatrix} \bar{f}_x^{+x} + \bar{f}_x^{-x} \\ \bar{f}_y^{+y} + \bar{f}_y^{-y} \\ \bar{f}_z^{+z} + \bar{f}_z^{-z} \end{bmatrix} \quad (4)$$

All model in parameters in equation 2 can be solved in a similar manner, which have all been listed in section 6.1.

1.2 Beyond Traditional IMU Calibration

While traditional calibration methods have proven successful over the past several decades, there is a push within the navigation community to move to systematic calibration methods [2, 12, 13, 14, 15, 16]. It is difficult to estimate more model parameters with the same limited dynamics, and the piece-meal approach to post-processing IMU calibration data is cumbersome and complicated. Additionally, traditional means of calibration do not provide any sort of measure of uncertainty which many navigation algorithms (i.e., Kalman filters) require for any sort of state estimation.

Therefore, this paper aims to investigate systematic IMU calibration through the lens of inverse problem techniques. A comparison of a systematic formulation of IMU calibration will be compared to the traditional approach. Also, new motion sequences for a single-axis as well as multiple axes will be explored. In addition, the inverse problem aims to be solved via weighted least squares to then provide some measure of uncertainty for the estimated model parameters.

2 Methods

Consider an IMU under test strapped down to a three axis rotational test bed. The rotational test bed provides measurements of angular position and angular rate along each test axis. As exemplar hardware, the unit under test will be a STIM 300 IMU from Safran and the 210C Series Three Axis Position and Rate Table System from Ideal Aerosmith.

2.1 STIM 300 IMU Specifications

The STIM 300 IMU, henceforth referred to as the unit under test (UUT), provides measurements of specific force and angular velocity. While the true forward model is unknown, it will be assumed that the basic forward model in equation 1 will sufficiently model the error of the device. Assuming the UUT uses the "10g" variant of accelerometers, bounds for the accelerometer-related model parameters are provided in table 5-5 of the specification sheet [17].

- Bias: $|b_a| \leq 7.5 \times 10^{-3}g$
- Scale Factor Error : $|s_a| \leq 200 \text{ ppm}$
- Misalignment: $|m_a| \leq 1 \times 10^{-3} \text{ rad}$

The accelerometers are also subject to zero-mean Gaussian noise with a velocity random walk (VRW) value of $0.07\text{m/s}/\sqrt{\text{Hz}}$, which translates to a $\sigma_a = \frac{0.07}{60} = 0.0012\text{ms}^{-1}$. Likewise, [17] provides bounds for the gyroscopes in table 5-3.

- Bias: $|b_g| \leq 250^\circ \text{ h}^{-1}$
- Scale Factor Error : $|s_g| \leq 500 \text{ ppm}$
- Misalignment: $|m_g| \leq 1 \times 10^{-3} \text{ rad}$

The gyroscopes are also subject to zero-mean Gaussian noise with an angle random walk (ARW) value of $0.15^\circ/\sqrt{\text{h}}$ which translates to a $\sigma_g = \frac{0.15}{60} \frac{\pi}{180} = 4.3633 \times 10^{-5} \text{ rad s}^{-1}$.

For simulation purposes, true model parameters will be selected within these bounds.

2.2 Simulating Calibration Data and Model Parameters

Rotational motion on the test bed will be simulated by developing a true sequence of angular velocities $\boldsymbol{\omega}$ across time t experienced by the UUT. The attitude of the UUT, represented by the direction cosine matrix $C(t)$, will be integrated in discrete steps such that the k^{th} step in the sequence is

$$C(t_k) = C_0 \prod_{i=1}^k e^{[\boldsymbol{\omega}(t_i) \times] \Delta t} \quad (5)$$

where $[\boldsymbol{\omega}(t_i) \times]$ is a skew-symmetric matrix and Δt is the time step. While the test bed rotates, the accelerometers will each be measuring components of the normal force from the test bed resulting

from the acceleration due to gravity g . For each time step k , the true specific force quantity is given below.

$$\mathbf{f}(t_k) = C(t_k) \begin{bmatrix} 0 \\ 0 \\ g \end{bmatrix} \quad (6)$$

In the simulation, it will be assumed that quantities $\boldsymbol{\omega}$ and \mathbf{f} will be available through measurement outputs of the test bed itself. Measurements of these quantities from the UUT will be corrupted with measurement error according to equations 2. The values of the model parameters are recorded in table 2 and are selected with reasonable orders of magnitude as discussed in section 2.1.

| Model Parameter | Accel Values | Gyro Values |
|----------------------|----------------------------|---|
| Fixed Bias X | 0.0628 m s^{-2} | $0.48481 \times 10^{-3} \text{ rad s}^{-1}$ |
| Fixed Bias Y | -0.0510 m s^{-2} | $0.14544 \times 10^{-3} \text{ rad s}^{-1}$ |
| Fixed Bias Z | 0.0363 m s^{-2} | $1.2120 \times 10^{-3} \text{ rad s}^{-1}$ |
| Scale Factor Error X | 150 ppm | 450 ppm |
| Scale Factor Error Y | -175 ppm | -300 ppm |
| Scale Factor Error Z | 198 ppm | 175 ppm |
| Misalignment XY | 0.1 mrad | -0.1 mrad |
| Misalignment XZ | -0.2 mrad | 0.2 mrad |
| Misalignment YX | 0.3 mrad | -0.3 mrad |
| Misalignment YZ | -0.4 mrad | 0.4 mrad |
| Misalignment ZX | 0.5 mrad | -0.5 mrad |
| Misalignment ZY | -0.6 mrad | 0.6 mrad |

Table 2: UUT Simulated Model Parameters

Capabilities for simulating calibration sequences on test beds and IMU error models have been developed in MATLAB®.

2.3 Formulating IMU Calibration as a Discrete Linear Inverse Problem

Recall the system of equations from equation 2 and consider the x -axis accelerometer measurements.

$$\tilde{f}_x = (1 + s_{a,x}) f_x + m_{a,xy} f_y + m_{a,xz} f_z + b_{a,x}$$

The equation above can be re-arranged to express the model parameters as a function of the accelerometer error $\Delta f = \tilde{f} - f$.

$$\tilde{f}_x = (1 + s_{a,x}) f_x + m_{a,xy} f_y + m_{a,xz} f_z + b_{a,x}$$

$$\tilde{f}_x - f_x = b_{a,x} + s_{a,x} f_x + m_{a,xy} f_y + m_{a,xz} f_z$$

$$\Delta f_x = b_{a,x} + s_{a,x}f_x + m_{a,xy}f_y + m_{a,xz}f_z$$

Assuming that both the UUT and test bed are able to provide synchronized measurements at the same sampling frequency, a series of measurements from these devices can be organized into another system of equations.

$$\begin{bmatrix} 1 & f_x[1] & f_y[1] & f_z[1] \\ 1 & f_x[2] & f_y[2] & f_z[2] \\ \vdots & \vdots & \vdots & \vdots \\ 1 & f_x[m] & f_y[m] & f_z[m] \end{bmatrix} \begin{bmatrix} b_{a,x} \\ s_{a,x} \\ m_{a,xy} \\ m_{a,xz} \end{bmatrix} = \begin{bmatrix} \Delta f_x[1] \\ \Delta f_x[2] \\ \vdots \\ \Delta f_x[m] \end{bmatrix} \quad (7)$$

This system of equations can be expressed in the form $G\mathbf{m} = \mathbf{d}$. In this expression, "true" measurements $f_x[n]$, $f_y[n]$, $f_z[n]$ within the model operator are computed from measurements provided by the test bed, and the model parameters are various calibration factors from the forward model. Elements of the data vector \mathbf{d} are the difference of the UUT output and test bed output such that $d[n] = \tilde{f}_x[n] - f_x[n]$.

Let F be the model operator demonstrated by equation 7.

$$F := \begin{bmatrix} 1 & f_x[1] & f_y[1] & f_z[1] \\ 1 & f_x[2] & f_y[2] & f_z[2] \\ \vdots & \vdots & \vdots & \vdots \\ 1 & f_x[m] & f_y[m] & f_z[m] \end{bmatrix}, \quad F \in \mathbb{R}^{m \times 4} \quad (8)$$

Then, the discrete linear inverse problem for all accelerometer calibration parameters given in equation 2 can be defined below.

$$G_a \mathbf{m}_a = \mathbf{d}_a \quad (9)$$

$$\begin{bmatrix} F & 0_{m \times 4} & 0_{m \times 4} \\ 0_{m \times 4} & F & 0_{m \times 4} \\ 0_{m \times 4} & 0_{m \times 4} & F \end{bmatrix} \begin{bmatrix} b_{a,x} \\ s_{a,x} \\ m_{a,xy} \\ m_{a,xz} \\ b_{a,y} \\ m_{a,yz} \\ s_{a,y} \\ m_{a,yz} \\ b_{a,z} \\ m_{a,zx} \\ m_{a,zy} \\ s_{a,z} \end{bmatrix} = \begin{bmatrix} \Delta f_x[1] \\ \vdots \\ \Delta f_x[m] \\ \Delta f_y[1] \\ \vdots \\ \Delta f_y[m] \\ \Delta f_z[1] \\ \vdots \\ \Delta f_z[m] \end{bmatrix}$$

Likewise, let Ω be the model operator for all gyroscope measurements specific to one sensor.

$$\Omega := \begin{bmatrix} 1 & \omega_x[1] & \omega_y[1] & \omega_z[1] \\ 1 & \omega_x[2] & \omega_y[2] & \omega_z[2] \\ \vdots & \vdots & \vdots & \vdots \\ 1 & \omega_x[m] & \omega_y[m] & \omega_z[m] \end{bmatrix}, \quad \Omega \in \mathbb{R}^{m \times 4} \quad (10)$$

Then, the discrete linear inverse problem for all gyroscope calibration parameters given in equation 2 can be defined below.

$$G_g \mathbf{m}_g = \mathbf{d}_g \quad (11)$$

$$\begin{bmatrix} \Omega & 0_{m \times 4} & 0_{m \times 4} \\ 0_{m \times 4} & \Omega & 0_{m \times 4} \\ 0_{m \times 4} & 0_{m \times 4} & \Omega \end{bmatrix} \begin{bmatrix} b_{g,x} \\ s_{g,x} \\ m_{g,xy} \\ m_{g,xz} \\ b_{g,y} \\ m_{g,yz} \\ s_{g,y} \\ m_{g,yz} \\ b_{g,z} \\ m_{g,zx} \\ m_{g,zy} \\ s_{g,z} \end{bmatrix} = \begin{bmatrix} \Delta\omega_x[1] \\ \vdots \\ \Delta\omega_x[m] \\ \Delta\omega_y[1] \\ \vdots \\ \Delta\omega_y[m] \\ \Delta\omega_z[1] \\ \vdots \\ \Delta\omega_z[m] \end{bmatrix}$$

2.4 Assessing Singular Values

Prior to solving the inverse problem, we must ensure that the problem is not ill-conditioned. This is accomplished by performing a singular value decomposition (SVD) on the model operators Ω and F respectively from equations 10 and 8. Although these model operators may appear to be full-rank when calling MATLAB[®]'s `rank()` function, some singular values may be poorly scaled. Therefore, it is essential to verify that the singular values are suitable for each new motion profile run on the three-axis rate table.

If the singular values are poorly scaled, it may be necessary to compute a truncated SVD solution or regularize the solution. In both cases, this takes away the opportunity to assess the resulting covariances and correlations between model parameters as the model null-space is now non-trivial and may lead to a biased solution in the model parameters.

2.5 L2 Regression without a Known Normal Distribution

Although a typical IMU specification sheet contains values of VRW and ARW which relate to the white noise present on each sensor channel, in practice each individual sensor is subject to its own amount of white noise. Therefore, to be consistent with application, we will assume that each sample is dependent and identically distributed, although the standard deviation associated with the white noise will be unknown. Therefore, casting this problem as a weighted least squares

problem is not feasible. Additionally in practice, it is not a safe assumption to assume that the power of the white noise signal is equally distributed at all frequencies, introducing noise color, however this will be ignored for both simulation and evaluation purposes.

Since the inverse problem can not be casted as a weighted least squares problem, the inverse problem will be solved via the normal equations (assuming the model operator is not ill-conditioned) without any scaling applied to the model operators.

$$\mathbf{m}_{a,L2} = (G_a^T G_a)^{-1} G_a^T \mathbf{d}_a \quad (12)$$

$$\mathbf{m}_{g,L2} = (G_g^T G_g)^{-1} G_g^T \mathbf{d}_g$$

Without a known standard deviation, we instead must estimate the resulting standard deviation from the residuals after performing the least squares fit.

$$s_a = \frac{\|G_a \mathbf{m}_{a,L2} - \mathbf{d}_a\|_2}{\sqrt{m-n}} \quad (13)$$

$$s_g = \frac{\|G_g \mathbf{m}_{g,L2} - \mathbf{d}_g\|_2}{\sqrt{m-n}}$$

With these estimated standard deviations, we can approximate the model covariance.

$$\tilde{C}_a = s_a^2 (G_a^T G_a)^{-1} \quad (14)$$

$$\tilde{C}_g = s_g^2 (G_g^T G_g)^{-1}$$

Rather than using a Normal distribution to determine the 95% confidence interval, we must use the Student's t distribution instead. In this use case, the degree of freedom will be very large which should well-approximate the normal distribution.

$$m_{a,L2_i} \pm t_{0.95,\nu} \sqrt{\tilde{C}_{a_i,i}} \quad (15)$$

$$m_{g,L2_i} \pm t_{0.95,\nu} \sqrt{\tilde{C}_{g_i,i}}$$

In addition to the model covariance, the correlation between each model parameter will also be examined.

2.6 Motion Profile Evaluation

First, we will investigate using traditional calibration data to solve the inverse problem and make comparisons to the traditional post-processing methods for IMU calibration.

Then, we will investigate three unique motion profiles for evaluation.

1. Single-Axis Tilts in One Direction
2. Single-Axis Tilts in Two Directions
3. Multi-Axis Tilts in All Directions

The dynamics of each motion profile will cause varying model fits, covariances, and correlations. These insights will be useful to those needing to develop new motion profiles to calibrate IMUs. Their Euler angle profiles are proved in figures 2, 3, and 4.

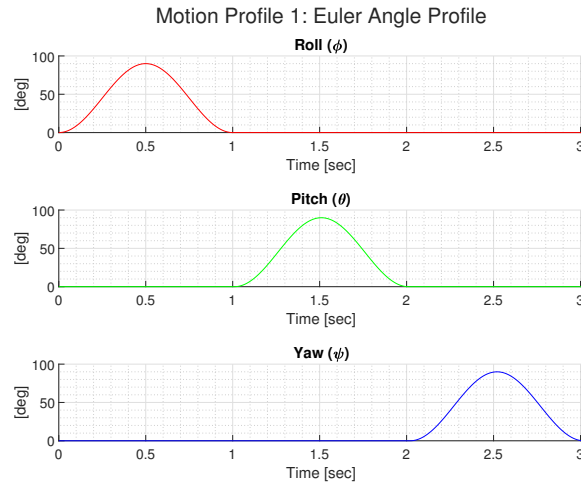


Figure 2: Motion Profile 1: Euler Angle Profile

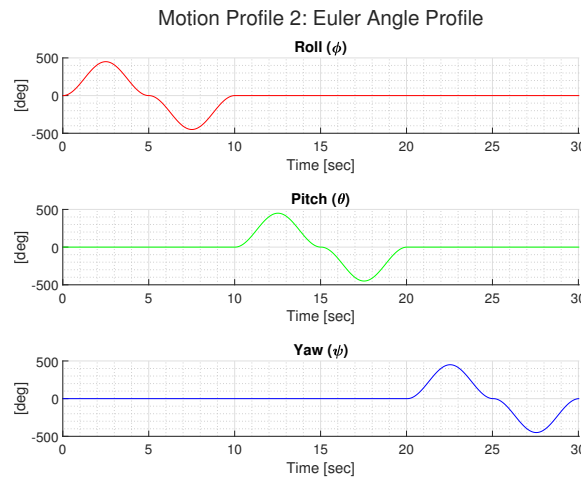


Figure 3: Motion Profile 2: Euler Angle Profile

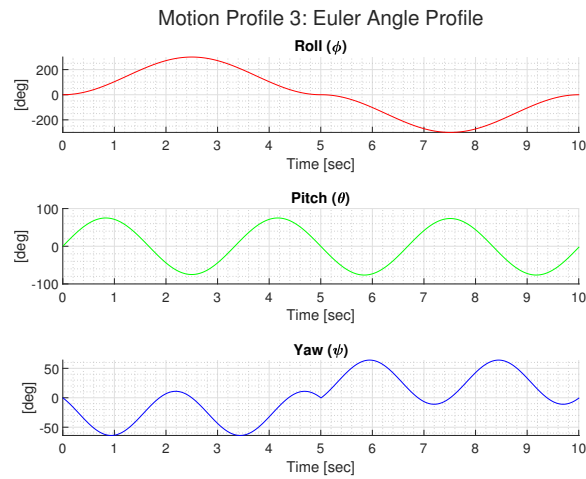


Figure 4: Motion Profile 3: Euler Angle Profile

Then, we will analyze a motion profile designed to purposely be ill-conditioned to determine what model fit, if any, could be obtained if forced into this situation. This motion profile is provided in figure 5.

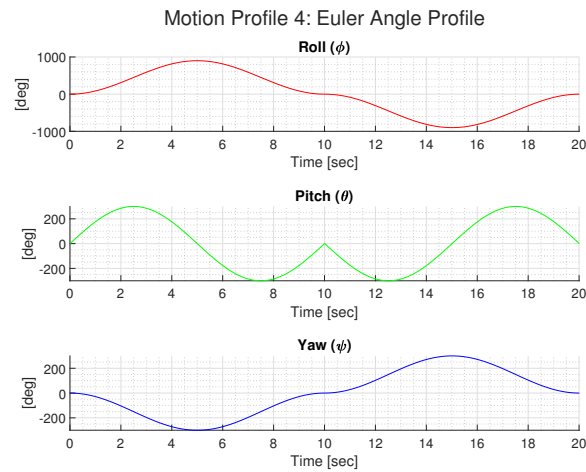


Figure 5: Motion Profile 3: Euler Angle Profile

Comparisons between all the utilized methods will be provided in section 4.

3 Results

The following sections contain the results of each motion profile evaluation.

3.1 Traditional Calibration Sequence

A traditional calibration sequence was simulated for a UUT with an assumed sample rate of 100 Hz. Each test specified in table 1 for a duration of 10 s. All of the accelerometer test data were appended together to build the model operator G_a , and as well as all of the gyroscope test data to build G_g . Each model operator contains 12 columns. Before solving the least squares problem, the singular values were assessed for each model operator as shown in figures 6 and 7.

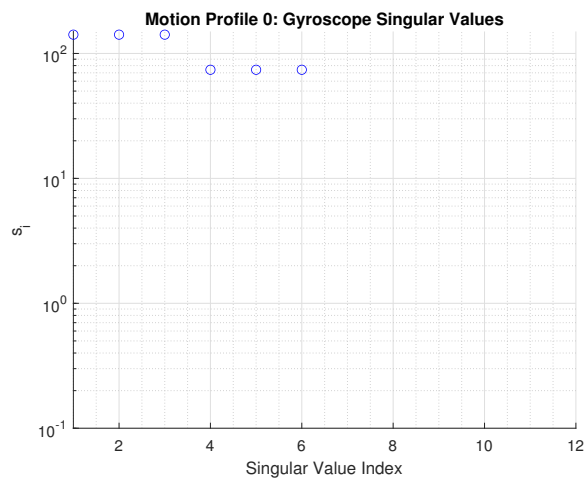


Figure 6: Traditional Motion Profile - Gyroscope Singular Values

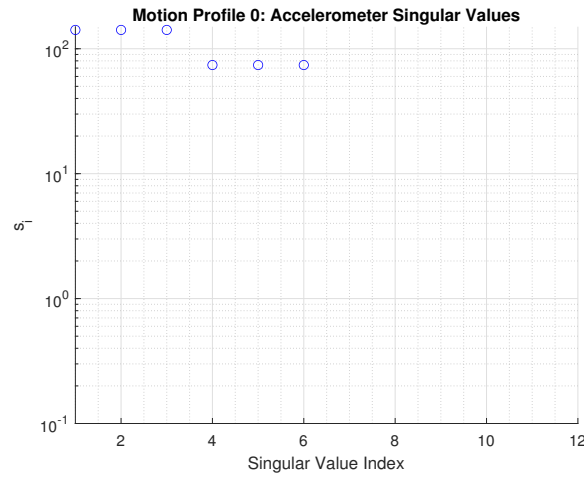


Figure 7: Traditional Motion Profile - Accelerometer Singular Values

For both G_g and G_a , there are six singular values that equal 0, meaning that each model operator is not full rank! This means the products $G_g^T G_g$ and $G_a^T G_a$ are not invertable, meaning that the normal equations can not be solved. Rather than trying to regularize the solution, it was decided to instead abandon this comparison and instead evaluate new motion profiles for the three-axis rate table that will result in full rank model operators.

3.2 New Motion Profile Evaluation

In light of the fact that the traditional motion profile does not yield a full rank model operator, new motion profiles were investigated. It would take a significantly long time to exhaust every possible motion profile for rotating an IMU through every possible attitude, therefore three motion profiles were selected for evaluation.

1. **Single-Axis Tilts in One Direction**
2. **Single-Axis Tilts in Two Directions**
3. **Multi-Axis Tilts in All Directions**

The following subsections contain results for each motion profile.

3.2.1 Motion Profile 1: Single-Axis Tilts in One Direction

This motion profile resulted in the following angular velocity profile and gyroscope measurement error shown in the figure below.

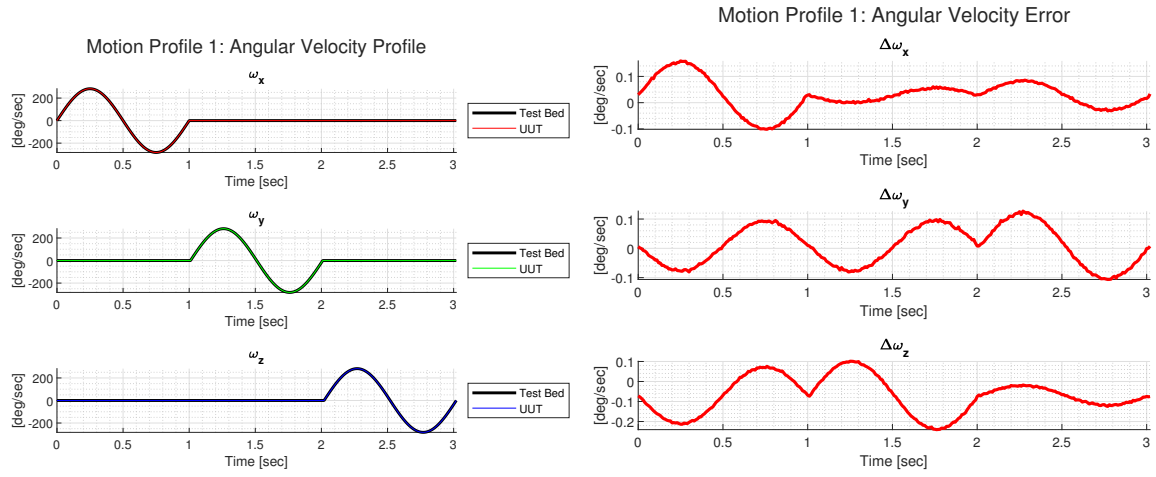


Figure 8: Motion Profile 1 - Angular Velocity Profile

In addition, the resulting specific force profile due to the rotation of the IMU through the local gravity field is shown in the figure below.

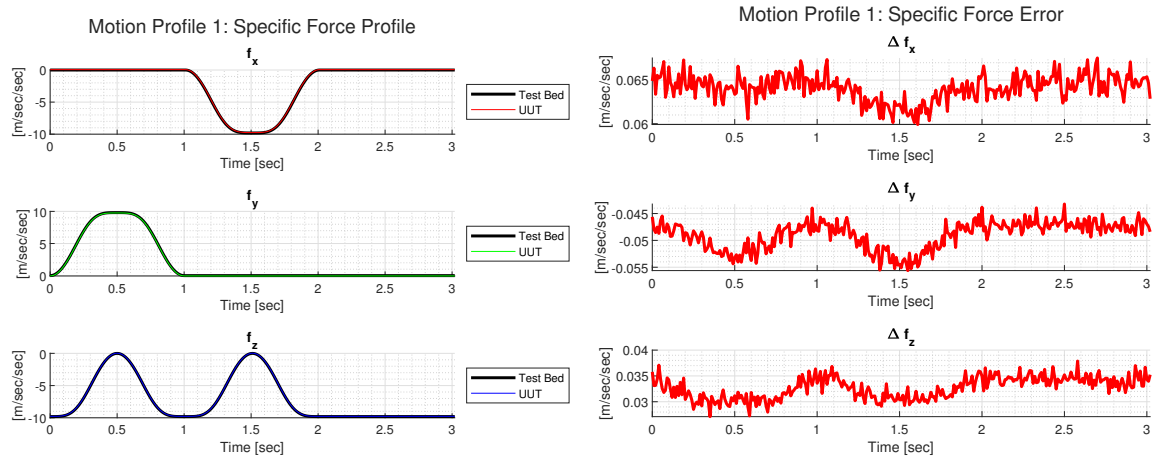


Figure 9: Motion Profile 1 - Specific Force Profile

Prior to solving the normal equations, the singular values for both model operators G_g and G_a were visually inspected to ensure each were well-conditioned.

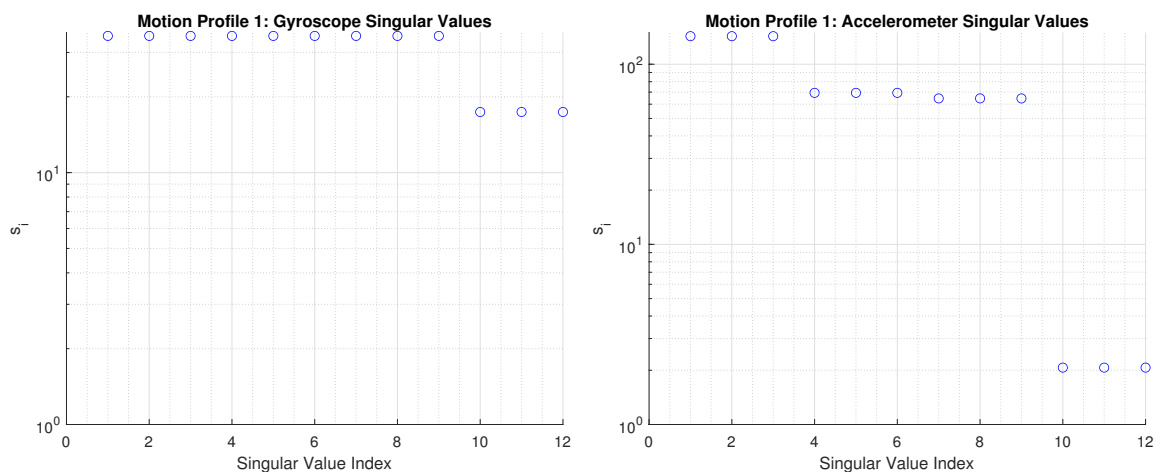


Figure 10: Motion Profile 1 - Singular Values

Following the process discussed in section 2.5, the following results were achieved for the gyroscope and accelerometer calibrations.

| Motion Profile 1: Gyroscope Calibration Results | | | | | |
|---|------------|-------------|-------------|------------|--------------|
| | TrueModel | L2Model | ModelError | Covariance | Confidence95 |
| GyroFixedBiasX | 0.00048481 | 0.00048732 | 2.5038e-06 | 6.4151e-12 | 2.0992e-06 |
| GyroScaleFactorErrorX | 0.00045 | 0.00045145 | 1.4511e-06 | 1.5964e-12 | 1.0472e-06 |
| GyroMisalignmentXY | -0.0001 | -0.00010103 | -1.0317e-06 | 1.5964e-12 | 1.0472e-06 |
| GyroMisalignmentXZ | 0.0002 | 0.00020003 | 2.7266e-08 | 1.5964e-12 | 1.0472e-06 |
| GyroFixedBiasY | 0.00014544 | 0.00014622 | 7.7278e-07 | 6.4151e-12 | 2.0992e-06 |
| GyroMisalignmentYX | -0.0003 | -0.0002994 | 5.9932e-07 | 1.5964e-12 | 1.0472e-06 |
| GyroScaleFactorErrorY | -0.0003 | -0.00030175 | -1.754e-06 | 1.5964e-12 | 1.0472e-06 |
| GyroMisalignmentYZ | 0.0004 | 0.00039947 | -5.261e-07 | 1.5964e-12 | 1.0472e-06 |
| GyroFixedBiasZ | -0.001212 | -0.0012133 | -1.2866e-06 | 6.4151e-12 | 2.0992e-06 |
| GyroMisalignmentZX | -0.0005 | -0.00049914 | 8.6363e-07 | 1.5964e-12 | 1.0472e-06 |
| GyroMisalignmentZY | 0.0006 | 0.00060153 | 1.5348e-06 | 1.5964e-12 | 1.0472e-06 |
| GyroScaleFactorErrorZ | 0.000175 | 0.00017451 | -4.8574e-07 | 1.5964e-12 | 1.0472e-06 |

Figure 11: Motion Profile 1 - Gyroscope Calibration Results

| | TrueModel | L2Model | ModelError | Covariance | Confidence95 |
|------------------------|-----------|-------------|-------------|------------|--------------|
| AccelFixedBiasX | 0.062784 | 0.063016 | 0.00023226 | 2.828e-07 | 0.00044076 |
| AccelScaleFactorErrorX | 0.00015 | 0.00018966 | 3.9658e-05 | 2.0107e-09 | 3.7164e-05 |
| AccelMisalignmentXY | 0.0001 | 5.7749e-05 | -4.2251e-05 | 2.0107e-09 | 3.7164e-05 |
| AccelMisalignmentXZ | -0.0002 | -0.00019111 | 8.8872e-06 | 2.5685e-09 | 4.2005e-05 |
| AccelFixedBiasY | -0.051012 | -0.050528 | 0.00048443 | 2.828e-07 | 0.00044076 |
| AccelMisalignmentYX | 0.0003 | 0.00031297 | 1.2968e-05 | 2.0107e-09 | 3.7164e-05 |
| AccelScaleFactorErrorY | -0.000175 | -0.00023134 | -5.6345e-05 | 2.0107e-09 | 3.7164e-05 |
| AccelMisalignmentYZ | -0.0004 | -0.00034876 | 5.1242e-05 | 2.5685e-09 | 4.2005e-05 |
| AccelFixedBiasZ | 0.036297 | 0.036148 | -0.0001491 | 2.828e-07 | 0.00044076 |
| AccelMisalignmentZX | 0.0005 | 0.00049392 | -6.0793e-06 | 2.0107e-09 | 3.7164e-05 |
| AccelMisalignmentZY | -0.0006 | -0.00058288 | 1.7117e-05 | 2.0107e-09 | 3.7164e-05 |
| AccelScaleFactorErrorZ | 0.000198 | 0.00017116 | -2.6837e-05 | 2.5685e-09 | 4.2005e-05 |

Figure 12: Motion Profile 1 - Accelerometer Calibration Results

In addition, the following model correlation matrices were achieved.

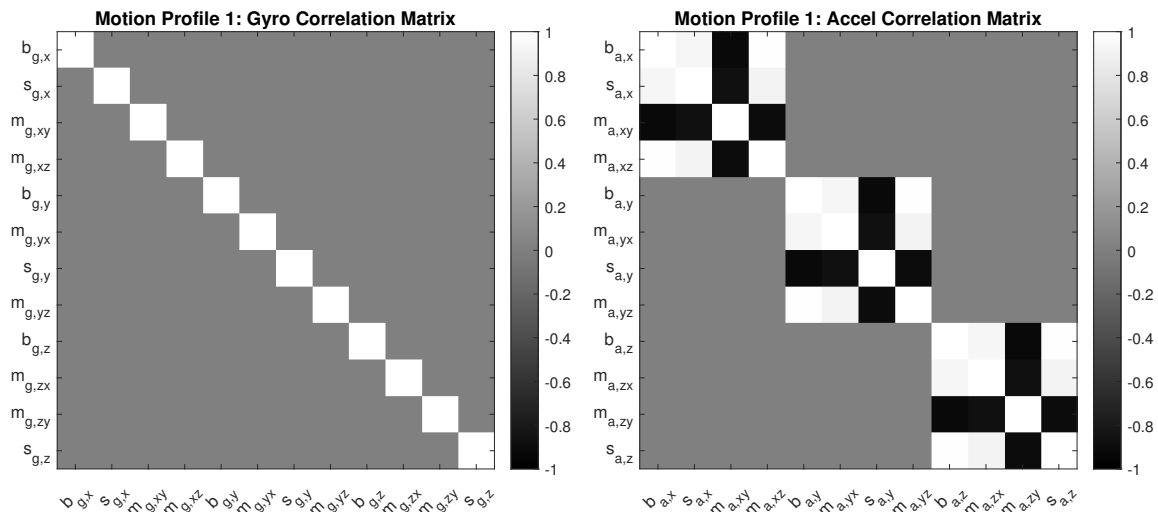


Figure 13: Motion Profile 1 - Correlation Matrices

3.2.2 Motion Profile 2: Single-Axis Tilts in Both Directions

This motion profile resulted in the following angular velocity profile and gyroscope measurement error shown in the figure below.

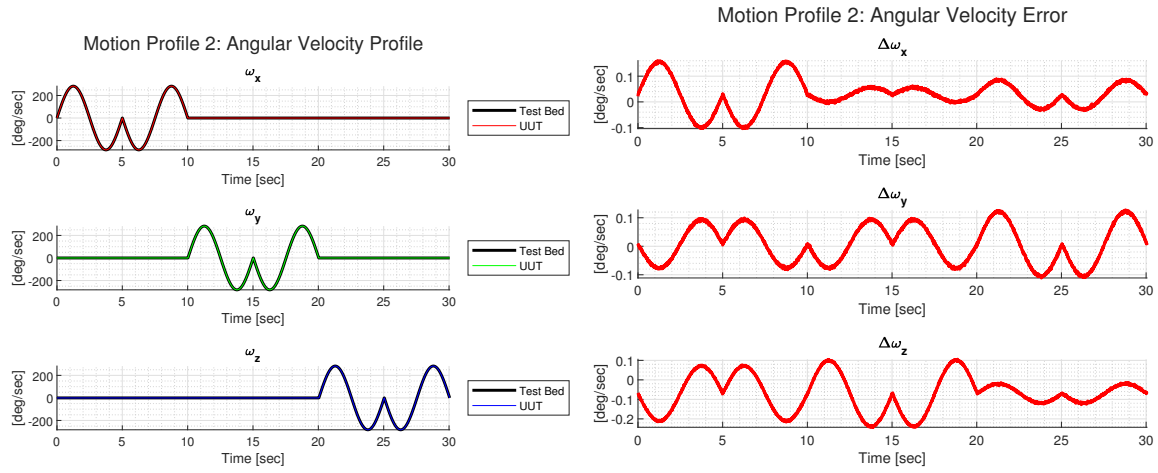


Figure 14: Motion Profile 2 - Angular Velocity Profile

In addition, the resulting specific force profile due to the rotation of the IMU through the local gravity field is shown in the figure below.

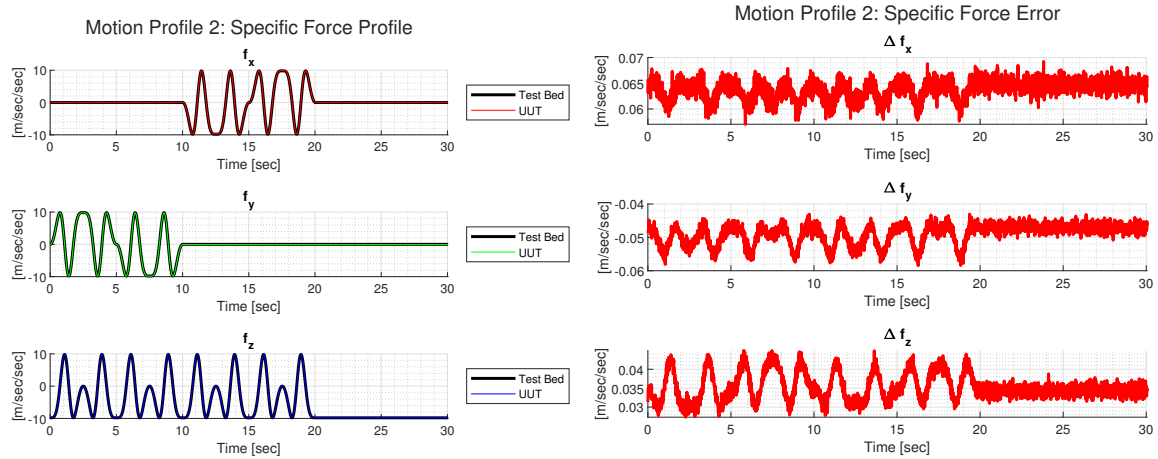


Figure 15: Motion Profile 2 - Specific Force Profile

Prior to solving the normal equations, the singular values for both model operators G_g and G_a were visually inspected to ensure each were well-conditioned.

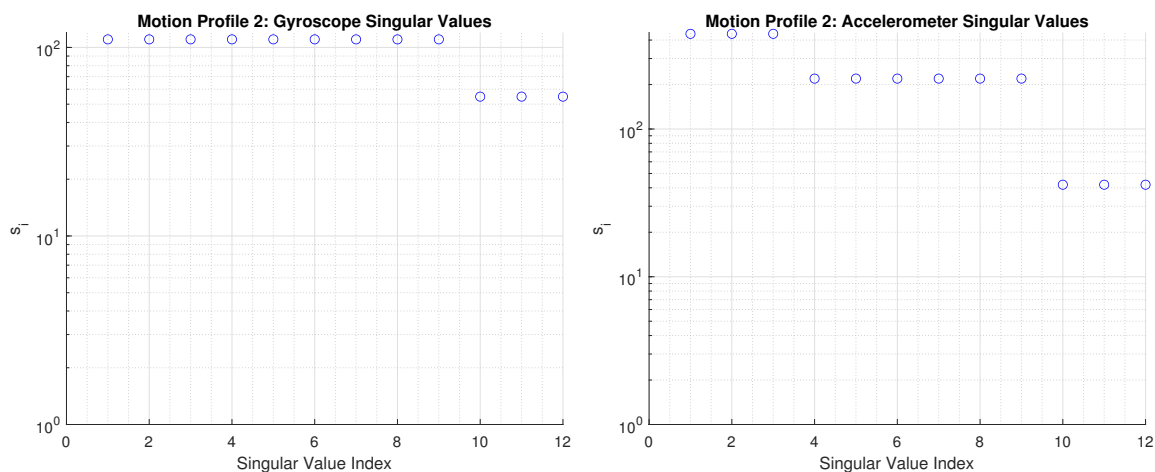


Figure 16: Motion Profile 2 - Singular Values

Following the process discussed in section 2.5, the following results were achieved for the gyroscope and accelerometer calibrations.

| Motion Profile 2: Gyroscope Calibration Results | | | | | |
|---|------------|-------------|-------------|------------|--------------|
| | TrueModel | L2Model | ModelError | Covariance | Confidence95 |
| GyroFixedBiasX | 0.00048481 | 0.00048409 | -7.2807e-07 | 6.3359e-13 | 6.5981e-07 |
| GyroScaleFactorErrorX | 0.00045 | 0.0004499 | -1.0447e-07 | 1.5642e-13 | 3.2784e-07 |
| GyroMisalignmentXY | -0.0001 | -0.00010027 | -2.6994e-07 | 1.5642e-13 | 3.2784e-07 |
| GyroMisalignmentXZ | 0.0002 | 0.00019953 | -4.6886e-07 | 1.5642e-13 | 3.2784e-07 |
| GyroFixedBiasY | 0.00014544 | 0.00014666 | 1.2204e-06 | 6.3359e-13 | 6.5981e-07 |
| GyroMisalignmentYX | -0.0003 | -0.00030022 | -2.2051e-07 | 1.5642e-13 | 3.2784e-07 |
| GyroScaleFactorErrorY | -0.0003 | -0.00029949 | 5.1267e-07 | 1.5642e-13 | 3.2784e-07 |
| GyroMisalignmentYZ | 0.0004 | 0.00040005 | 5.3763e-08 | 1.5642e-13 | 3.2784e-07 |
| GyroFixedBiasZ | -0.001212 | -0.0012119 | 1.4538e-07 | 6.3359e-13 | 6.5981e-07 |
| GyroMisalignmentZX | -0.0005 | -0.00050017 | -1.6829e-07 | 1.5642e-13 | 3.2784e-07 |
| GyroMisalignmentZY | 0.0006 | 0.00060015 | 1.535e-07 | 1.5642e-13 | 3.2784e-07 |
| GyroScaleFactorErrorZ | 0.000175 | 0.00017476 | -2.3906e-07 | 1.5642e-13 | 3.2784e-07 |

Figure 17: Motion Profile 2 - Gyroscope Calibration Results

| Motion Profile 2: Accelerometer Calibration Results | | | | | |
|---|-----------|-------------|-------------|------------|--------------|
| | TrueModel | L2Model | ModelError | Covariance | Confidence95 |
| AccelFixedBiasX | 0.062784 | 0.06278 | -3.5666e-06 | 7.6031e-10 | 2.2857e-05 |
| AccelScaleFactorErrorX | 0.00015 | 0.00014548 | -4.5236e-06 | 2.8007e-11 | 4.3869e-06 |
| AccelMisalignmentXY | 0.0001 | 9.5984e-05 | -4.0163e-06 | 2.8007e-11 | 4.3869e-06 |
| AccelMisalignmentXZ | -0.0002 | -0.00019674 | 3.2579e-06 | 1.1839e-11 | 2.8522e-06 |
| AccelFixedBiasY | -0.051012 | -0.050995 | 1.6696e-05 | 7.6031e-10 | 2.2857e-05 |
| AccelMisalignmentYX | 0.0003 | 0.00029863 | -1.3746e-06 | 2.8007e-11 | 4.3869e-06 |
| AccelScaleFactorErrorY | -0.000175 | -0.00017081 | 4.1923e-06 | 2.8007e-11 | 4.3869e-06 |
| AccelMisalignmentYZ | -0.0004 | -0.00040094 | -9.3569e-07 | 1.1839e-11 | 2.8522e-06 |
| AccelFixedBiasZ | 0.036297 | 0.036287 | -1.0123e-05 | 7.6031e-10 | 2.2857e-05 |
| AccelMisalignmentZX | 0.0005 | 0.00049215 | -7.8545e-06 | 2.8007e-11 | 4.3869e-06 |
| AccelMisalignmentZY | -0.0006 | -0.00060087 | -8.6632e-07 | 2.8007e-11 | 4.3869e-06 |
| AccelScaleFactorErrorZ | 0.000198 | 0.00020043 | 2.4343e-06 | 1.1839e-11 | 2.8522e-06 |

Figure 18: Motion Profile 2 - Accelerometer Calibration Results

In addition, the following model correlation matrices were achieved.

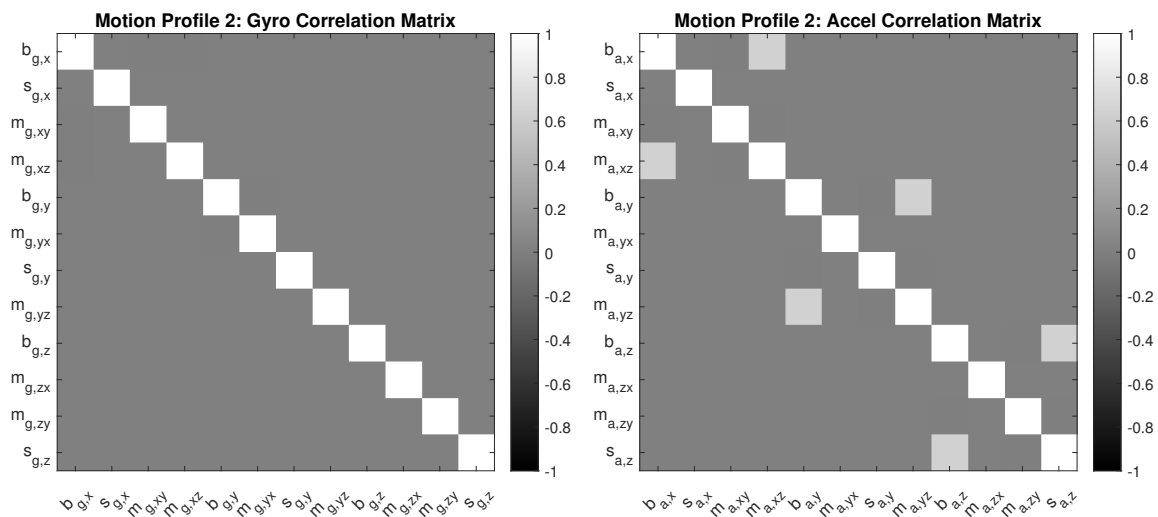


Figure 19: Motion Profile 2 - Correlation Matrices

3.2.3 Motion Profile 3: Multi-Axis Tilts in All Directions

This motion profile resulted in the following angular velocity profile and gyroscope measurement error shown in the figure below.

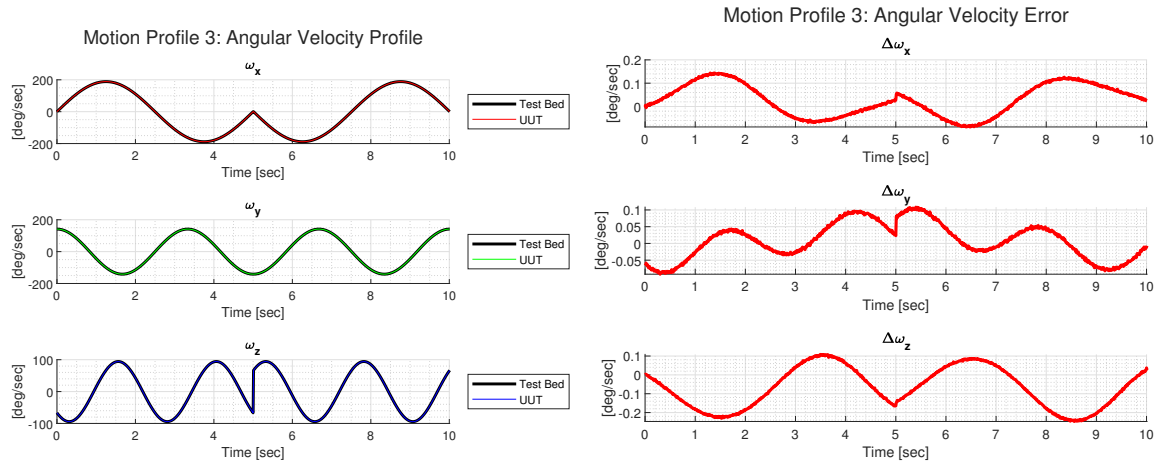


Figure 20: Motion Profile 3 - Angular Velocity Profile

In addition, the resulting specific force profile due to the rotation of the IMU through the local gravity field is shown in the figure below.

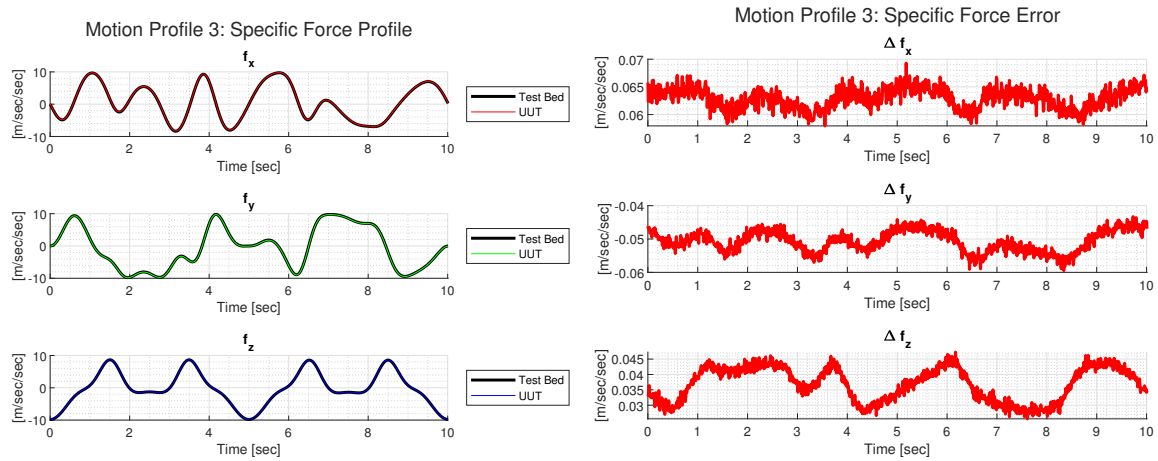


Figure 21: Motion Profile 3 - Specific Force Profile

Prior to solving the normal equations, the singular values for both model operators G_g and G_a were visually inspected to ensure each were well-conditioned.

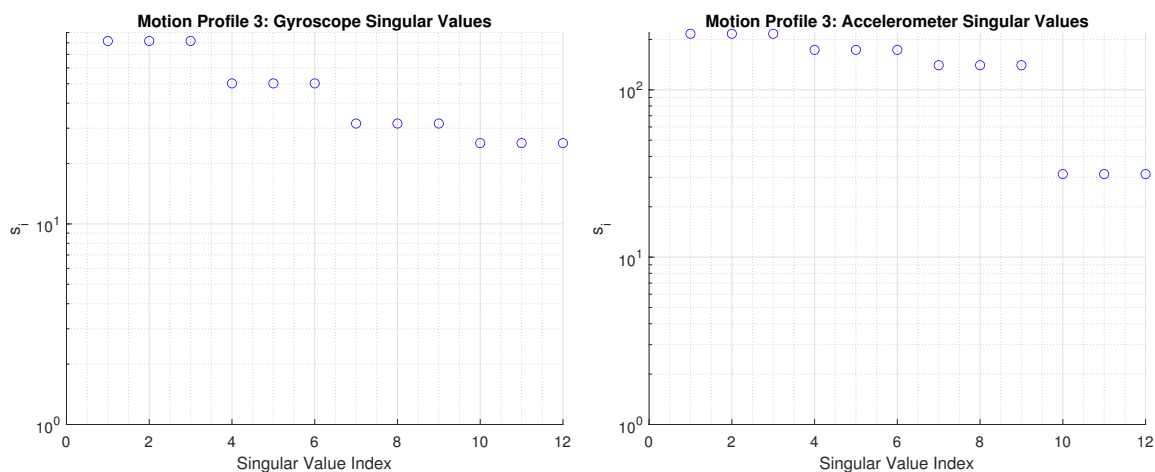


Figure 22: Motion Profile 3 - Singular Values

Following the process discussed in section 2.5, the following results were achieved for the gyroscope and accelerometer calibrations.

| Motion Profile 3: Gyroscope Calibration Results | | | | | |
|---|------------|-------------|-------------|------------|--------------|
| | TrueModel | L2Model | ModelError | Covariance | Confidence95 |
| GyroFixedBiasX | 0.00048481 | 0.00048638 | 1.5705e-06 | 1.9231e-12 | 1.1495e-06 |
| GyroScaleFactorErrorX | 0.00045 | 0.00044989 | -1.1346e-07 | 5.4832e-13 | 6.1379e-07 |
| GyroMisalignmentXY | -0.0001 | -0.00010035 | -3.4637e-07 | 1.3175e-12 | 9.5145e-07 |
| GyroMisalignmentXZ | 0.0002 | 0.00019989 | -1.1215e-07 | 2.2029e-12 | 1.2303e-06 |
| GyroFixedBiasY | 0.00014544 | 0.00014841 | 2.9625e-06 | 1.9231e-12 | 1.1495e-06 |
| GyroMisalignmentYX | -0.0003 | -0.00029947 | 5.3368e-07 | 5.4832e-13 | 6.1379e-07 |
| GyroScaleFactorErrorY | -0.0003 | -0.0002988 | 1.1953e-06 | 1.3175e-12 | 9.5145e-07 |
| GyroMisalignmentYZ | 0.0004 | 0.00040183 | 1.829e-06 | 2.2029e-12 | 1.2303e-06 |
| GyroFixedBiasZ | -0.001212 | -0.0012122 | -2.1024e-07 | 1.9231e-12 | 1.1495e-06 |
| GyroMisalignmentZX | -0.0005 | -0.00049927 | 7.3215e-07 | 5.4832e-13 | 6.1379e-07 |
| GyroMisalignmentZY | 0.0006 | 0.00059887 | -1.1344e-06 | 1.3175e-12 | 9.5145e-07 |
| GyroScaleFactorErrorZ | 0.000175 | 0.00017372 | -1.2787e-06 | 2.2029e-12 | 1.2303e-06 |

Figure 23: Motion Profile 3 - Gyroscope Calibration Results

| Motion Profile 3: Accelerometer Calibration Results | | | | | |
|---|-----------|-------------|-------------|------------|--------------|
| | TrueModel | L2Model | ModelError | Covariance | Confidence95 |
| AccelFixedBiasX | 0.062784 | 0.062867 | 8.2888e-05 | 1.3211e-09 | 3.0128e-05 |
| AccelScaleFactorErrorX | 0.00015 | 0.00014563 | -4.367e-06 | 4.8929e-11 | 5.7982e-06 |
| AccelMisalignmentXY | 0.0001 | 9.5679e-05 | -4.3206e-06 | 3.5822e-11 | 4.9611e-06 |
| AccelMisalignmentXZ | -0.0002 | -0.00019333 | 6.6675e-06 | 5.3017e-11 | 6.0355e-06 |
| AccelFixedBiasY | -0.051012 | -0.051016 | -3.6213e-06 | 1.3211e-09 | 3.0128e-05 |
| AccelMisalignmentYX | 0.0003 | 0.00029491 | -5.0948e-06 | 4.8929e-11 | 5.7982e-06 |
| AccelScaleFactorErrorY | -0.000175 | -0.00018297 | -7.9711e-06 | 3.5822e-11 | 4.9611e-06 |
| AccelMisalignmentYZ | -0.0004 | -0.00041711 | -1.7112e-05 | 5.3017e-11 | 6.0355e-06 |
| AccelFixedBiasZ | 0.036297 | 0.036319 | 2.1521e-05 | 1.3211e-09 | 3.0128e-05 |
| AccelMisalignmentZX | 0.0005 | 0.00050472 | 4.7164e-06 | 4.8929e-11 | 5.7982e-06 |
| AccelMisalignmentZY | -0.0006 | -0.00059413 | 5.8701e-06 | 3.5822e-11 | 4.9611e-06 |
| AccelScaleFactorErrorZ | 0.000198 | 0.00020554 | 7.543e-06 | 5.3017e-11 | 6.0355e-06 |

Figure 24: Motion Profile 3 - Accelerometer Calibration Results

In addition, the following model correlation matrices were achieved.

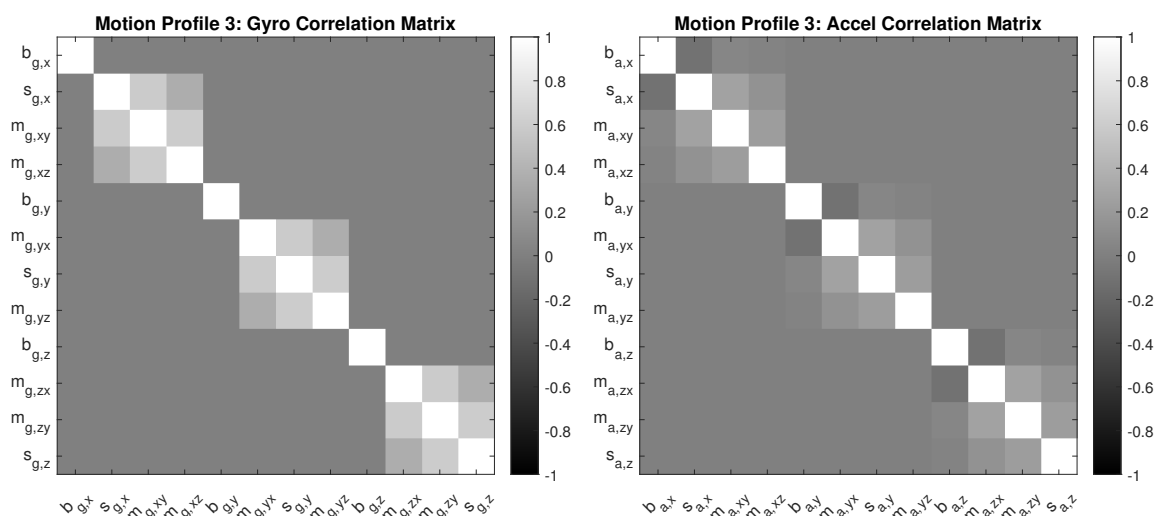


Figure 25: Motion Profile 3 - Correlation Matrices

3.3 IMU Calibration for Ill-Conditioned System Dynamics

A fourth motion profile was crafted to intentionally create an ill-conditioned model operator that could not be used in the methods covered in section 2.5. This motion profile resulted in the following angular velocity profile and gyroscope measurement error shown in the figure below.

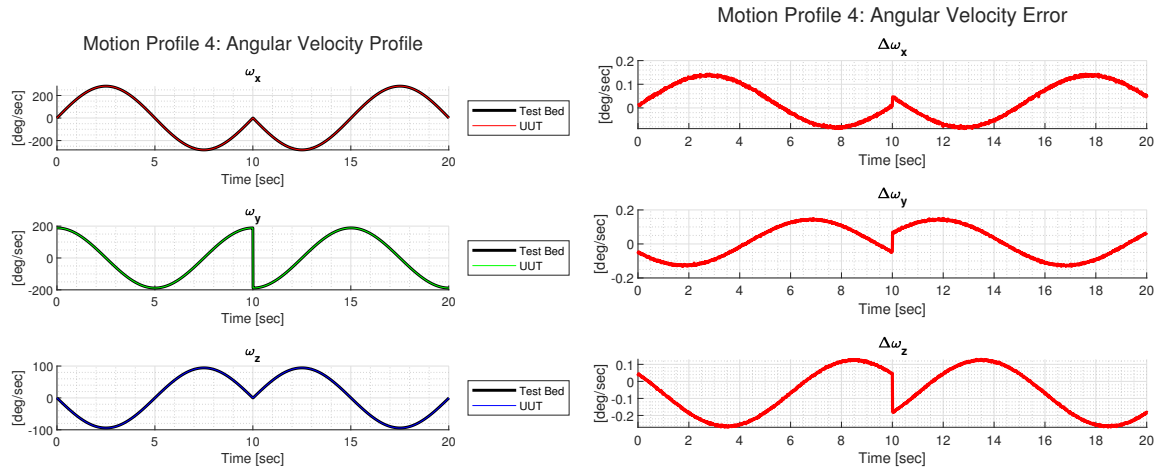


Figure 26: Motion Profile 4 - Angular Velocity Profile

In this case, the ill-conditioned model operator only applied to the gyroscope calibration, therefore we will only cover the results from this sensor suite.

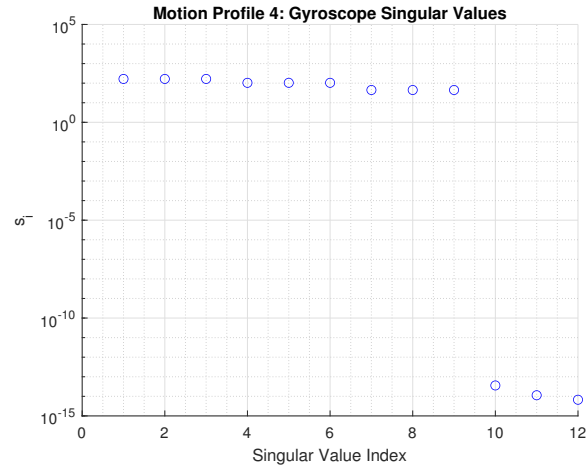


Figure 27: Motion Profile 4 - Gyroscope Singular Values

This is the situation when both the data and model null spaces are non-trivial, as the model operator contains 12 columns but is only of rank 9. The model null space is shown below in figure 28.

| Model Null Space | | |
|------------------|---------|---------|
| 0 | 0 | 0 |
| -0.3162 | 0 | 0 |
| -0.0000 | 0 | 0 |
| -0.9487 | 0 | 0 |
| 0 | 0 | 0 |
| 0 | -0.3162 | 0 |
| 0 | 0.0000 | 0 |
| 0 | -0.9487 | 0 |
| 0 | 0 | 0 |
| 0 | 0 | -0.3162 |
| 0 | 0 | 0.0000 |
| 0 | 0 | -0.9487 |

Figure 28: Motion Profile 4 - Model Null Space

The impact of this null space is also shown in the model resolution matrix, which is provided in figure 29. Notice that every odd index (i.e., 1, 3, 5, ...) of the model parameters are perfect resolved, but each even index (i.e., 2, 4, 6, ...) are subject to some sort of smearing. This is likely due to the specific dynamics chosen for this motion profile.

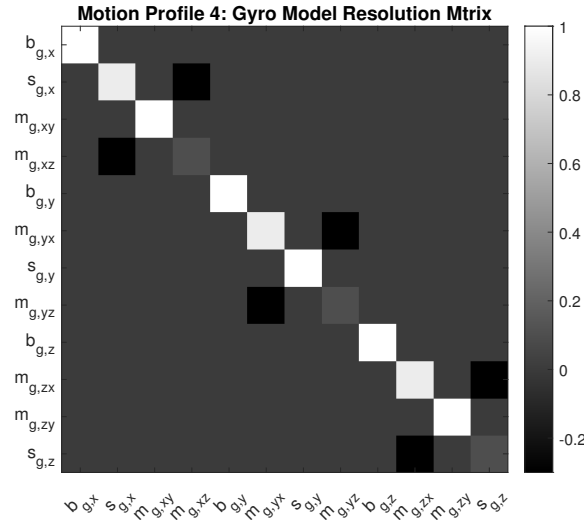


Figure 29: Motion Profile 4 - Gyroscope Model Resolution

The generalized pseudo-inverse is used to solve for a model of calibration parameters.

$$\mathbf{m}_{SVD} = G_g^\dagger \mathbf{d}_g = V_p S_p^{-1} U_p^T \mathbf{d}_g \quad (16)$$

Another means to solve for a model of calibration parameters is to apply Tikhonov regularization. In this case 0th-order Tikhonov regularization, also known as damped least squares, was utilized.

To select the damping parameter α , an L-curve was created to find the point at which both the model residuals and model norm are both minimized.

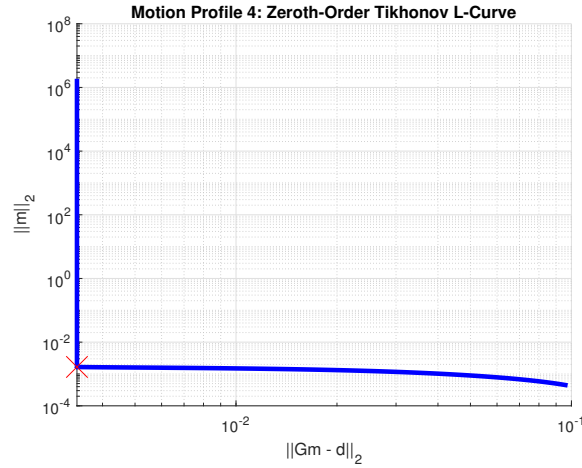


Figure 30: Motion Profile 4 - Tikhonov Regularization L-Curve

This point results in a value of $\alpha = 0.007824$. The solution \mathbf{m}_{tikh} is computed accordingly below.

$$\mathbf{m}_{tikh} = (G_g^T G_g + \alpha I)^{-1} G_g^T \mathbf{d}_g \quad (17)$$

The results for the two methods of solving for a calibration model in the presence of ill-conditioned model operators are below.

| Final Results | | | | | |
|-----------------------|------------|-------------|---------------|-------------|----------------|
| | TrueModel | SvdModel | SvdModelError | TikhModel | TikhModelError |
| GyroFixedBiasX | 0.00048481 | 0.00048498 | 1.6346e-07 | 0.00048498 | 1.6346e-07 |
| GyroScaleFactorErrorX | 0.00045 | 0.00034563 | -0.00010437 | 0.00034563 | -0.00010437 |
| GyroMisalignmentXY | -0.0001 | -9.9596e-05 | 4.0442e-07 | -9.9596e-05 | 4.0442e-07 |
| GyroMisalignmentXZ | 0.0002 | -0.00011521 | -0.00031521 | -0.00011521 | -0.00031521 |
| GyroFixedBiasY | 0.00014544 | 0.00014523 | -2.1676e-07 | 0.00014523 | -2.1676e-07 |
| GyroMisalignmentYX | -0.0003 | -0.00039006 | -9.0055e-05 | -0.00039006 | -9.0056e-05 |
| GyroScaleFactorErrorY | -0.0003 | -0.00030031 | -3.0951e-07 | -0.00030031 | -3.0951e-07 |
| GyroMisalignmentYZ | 0.0004 | 0.00013002 | -0.00026998 | 0.00013002 | -0.00026998 |
| GyroFixedBiasZ | -0.001212 | -0.0012116 | 4.2743e-07 | -0.0012116 | 4.2743e-07 |
| GyroMisalignmentZX | -0.0005 | -0.00050242 | -2.4208e-06 | -0.00050242 | -2.4206e-06 |
| GyroMisalignmentZY | 0.0006 | 0.00060001 | 1.0865e-08 | 0.00060001 | 1.0865e-08 |
| GyroScaleFactorErrorZ | 0.000175 | 0.00016747 | -7.5264e-06 | 0.00016747 | -7.526e-06 |

Figure 31: Motion Profile 4 - Gyroscope Calibration Results

Take notice that each method produced the same model.

4 Discussion

4.1 A Comparison to the Traditional Means of Calibration

It was unexpected that the model operators built from the traditional calibration data sets to be rank-deficient, blocking the opportunity to make a meaningful comparison. However, this obstacle is still impactful to the navigation community for those that have large amounts of legacy calibration data. This result implies that those that wish to upgrade to a systematic means of IMU calibration must collect new data with new motion profiles! The traditional methods for IMU calibration are not sufficient for systematic calibration.

4.2 A Comparison of the Three Motion Profiles

When designing new motion profiles to upgrade to systematic calibration, careful consideration is required to determine how the singular values, model errors, model covariances, and model parameter correlation are impacted. This comparison covers three different motion profiles. Each fitted model from the three motion profiles are compared in figure 32.

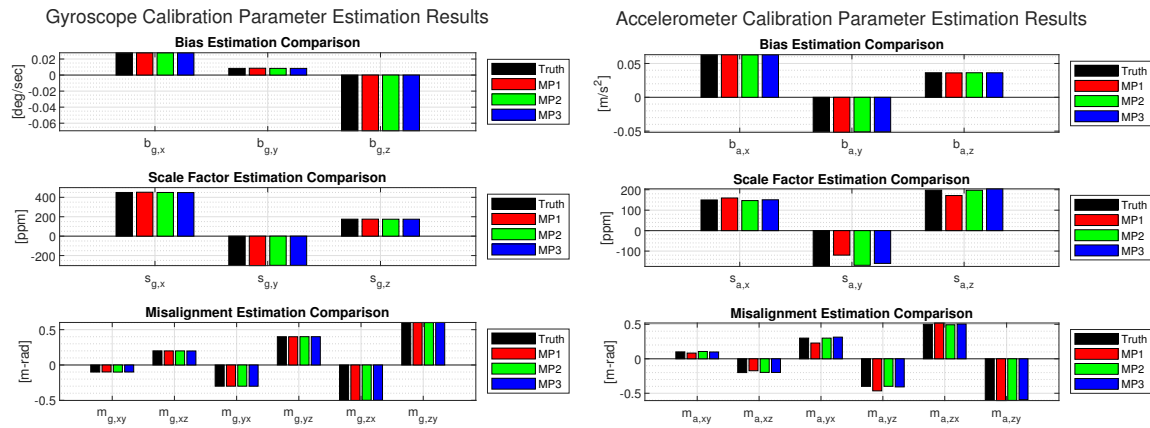


Figure 32: Calibration Parameter Comparison

Note that the least squares solution for each motion profile is relatively close to the true model parameters. In each case, there are no extreme outliers that indicate any large error. Similarly, figure 33 provides the error of each model parameter for each motion profile.

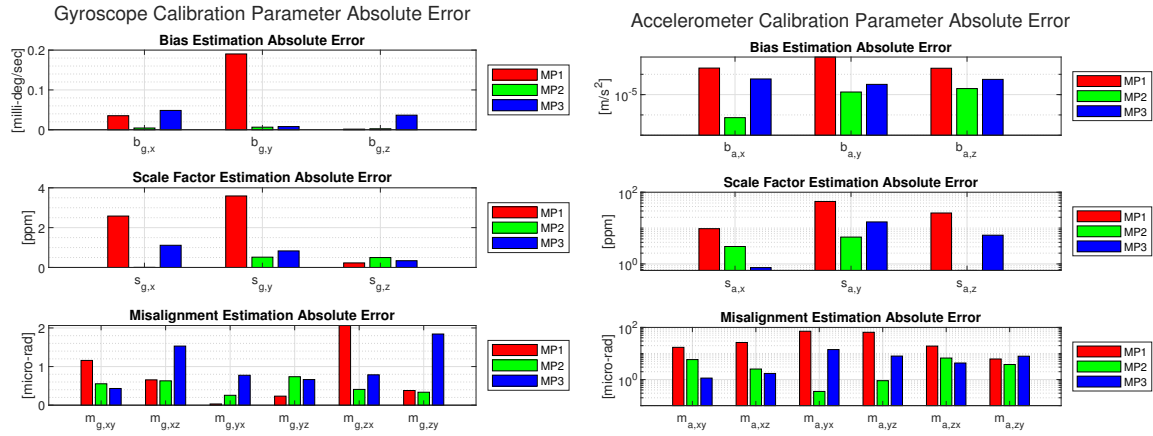


Figure 33: Calibration Parameter Error Comparison

In almost all cases, the second motion profile seems to yield the least amount of model error, while the first motion profile yields the most error. In a few cases the third motion profile outperforms the second motion profile, but it is surprising the third motion profile did not perform equally well. The model covariances and resulting confidence intervals follow a similar trend, shown in figures 34 and 35.

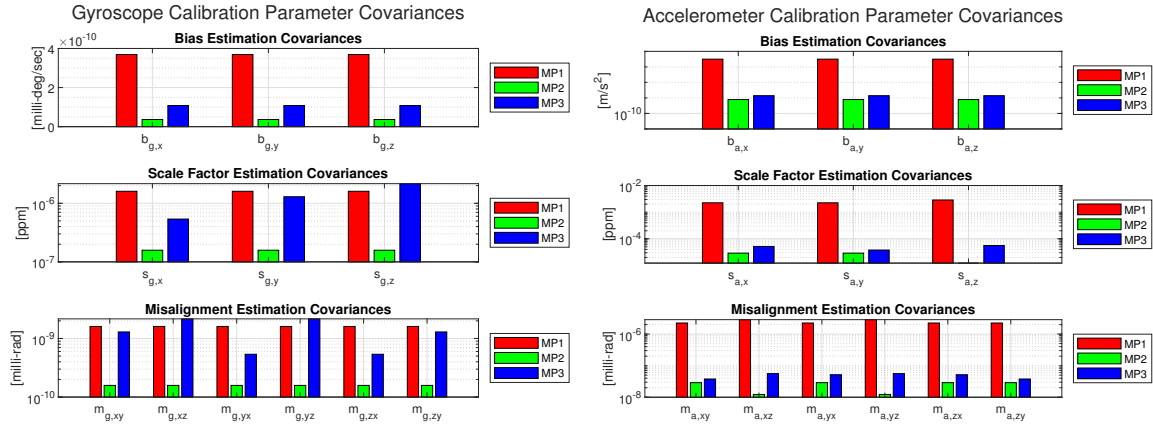


Figure 34: Calibration Parameter Covariance Comparison

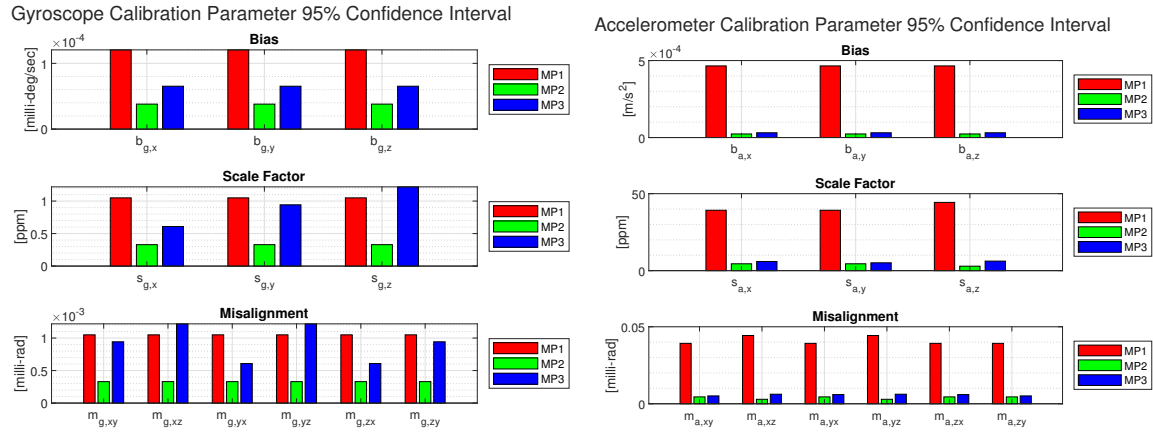


Figure 35: Calibration Parameter Confidence Interval Comparison

Notice that the covariances associated with the gyroscope scale factor and misalignment parameters are incredibly high, which is likely due to the correlation among these parameters shown in figure 25. This might also explain why the second motion profile yielded much better performance for the accelerometer parameters, which is when the least amount of parameter correlation was present as shown in figure 19. It seems that designing a motion profile that minimizes model parameter correlation is key to reducing the uncertainty for each calibration parameter. This insight is key for anyone calibrating IMUs for use in safety-critical systems where requirements may be stringent.

4.3 IMU Calibration for Ill-Conditioned System Dynamics

There may be situations where a three-axis rate table or other rotational test-bed may have limitations that could cause a situation for ill-conditioned model operators. Motion profile 4 was created to force this exact situation. Two methods, the truncated SVD and Tikhonov regularization, were applied to stabilize the solution. Figure 36 shows how each solution compares to the true model parameters.

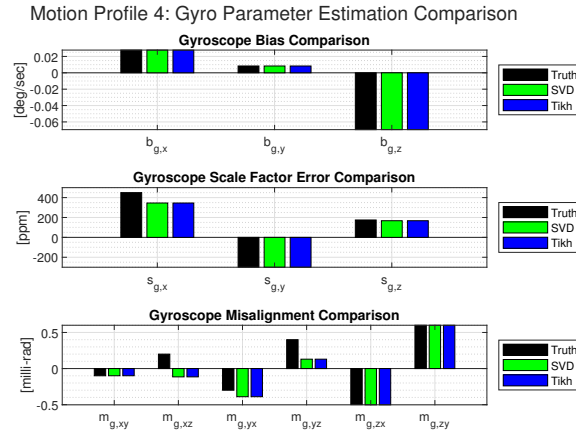


Figure 36: Motion Profile 4 - Model Parameter Comparison

Both methods were unable to solve parameters $m_{g,xz}$ and $m_{g,yz}$, which is consistent with the large values in the model null space shown in figure 28. However, some other model parameters still yielded decent solutions regardless of the model resolution. Interestingly, the error from each method were consistent with each other.

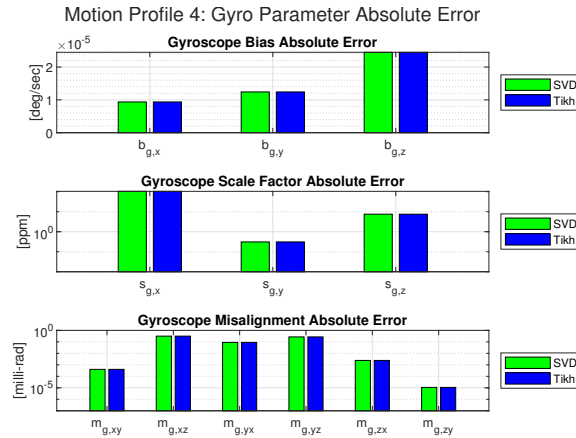


Figure 37: Motion Profile 4 - Model Parameter Error Comparison

The insight here is that attention needs to be brought to the model null space and resulting resolution matrix to understand how certain calibration parameters may be impacted. Although this situation may not be ideal, it is still possible to achieve some sort of a useful solution, even if it only provides a partial calibration of the sensor suite.

5 Conclusion

Inertial sensor calibration is an essential activity before installing an IMU into a self-driving vehicle for the purposes of navigation. Traditional calibration methods use simple tests on their respective rotational test beds and post-process the collected data in piece-meal sections to compute only the most basic of IMU error sources. In an effort to improve the status-quo, systematic calibration seeks to leverage batched estimation methods to extend model complexity and make use of all available information to estimate its model parameters. In addition, systematic calibration also establishes some measure of uncertainty for each model parameter which is useful for verifying the final calibration parameters used before vehicle application.

A direct comparison between traditional and systematic calibration could not be achieved due to the rank-deficient model operators constructed for systematic calibration. This implies that the traditional motion profiles used on a three-axis rate table are not sufficient for systematic calibration, which brings into question what motion profiles are suitable for meaningful systematic calibration.

In response, three motion profiles were created to test and evaluate of model accuracy and uncertainty are impacted. Overall, the second motion profile yielded the highest accuracy and smallest covariance, which was an unexpected result. This implies that more motion in a rotational test-bed is not always better. The key contributor to the second motion profile's performance is that the model parameters were subjected to smallest amount of correlation to each other. If someone were to continue the design of motion profiles to yield high-accuracy calibration, keeping model correlation in mind is key to success.

Each of the three motion profiles were designed to produce full-rank model operators, but a fourth motion profile was created to purposely create another rank-deficient situation. It was shown that the model null space was non-trivial, and the model resolution matrix made clear which model parameters were affected. Two methods, truncated-SVD and Tikhonov regularization, were utilized to stabilize the solution. Each method yielded the same results which lead to the same error. Some model parameters were able to be resolved perfectly, but others were shown to be far from the truth. There may be situations where these dynamics are unavoidable, but this work shows that there are still methods to develop a partial solution.

Overall, the benefits of systematic calibration over traditional calibration methods were demonstrated throughout this work. If careful consideration is given to the design of the motion profile, then systematic calibration can yield high-precision results with similar high-accuracy. In conclusion, this work provides a thorough proof-of-concept of strategies that could be adopted by inertial test laboratories to upgrade from traditional to systematic means of calibration.

References

- [1] P. Groves, *Principles of GNSS, Inertial, and Multisensor Integrated Navigation Systems, Second Edition*. GNSS/GPS, Artech House, 2013.
- [2] P. G. Savage, “Improved strapdown inertial measurement unit calibration procedures,” in *2018 IEEE/ION Position, Location and Navigation Symposium (PLANS)*, pp. 522–533, 2018.
- [3] “Ieee standard specification format guide and test procedure for linear single-axis, nongyroscopic accelerometers,” *IEEE Std 1293-2018 (Revision of IEEE Std 1293-1998)*, pp. 1–271, 2019.
- [4] “Ieee standard specification format guide and test procedure for coriolis vibratory gyros,” *IEEE Std 1431-2004*, pp. 1–78, 2004.
- [5] “Ieee standard for specifying and testing single-axis interferometric fiber optic gyros,” *IEEE Std 952-2020 (Revision of IEEE Std 952-1997)*, pp. 1–93, 2021.
- [6] “Ieee specification format for single-degree-of-freedom spring-restrained rate gyros,” *ANSI/IEEE Std 292-1969*, pp. 1–16, 1968.
- [7] “Ieee standard specification format guide and test procedure for single-degree-of-freedom rate-integrating gyros,” *IEEE Std 517-1974*, pp. 1–60, 1974.
- [8] “Ieee standard specification format guide and test procedure for single-axis laser gyros,” *IEEE Std 647-2006 (Revision of IEEE Std 647-1995)*, pp. 1–96, 2006.
- [9] “Ieee specification format guide and test procedure for two-degree-of-freedom dynamically tuned gyros,” *ANSI/IEEE Std 813-1988*, pp. 1–68, 1989.
- [10] D. L. Olson, J. Bingham, and M. R. Walker, “A generalized imu modeling framework for varying inertial sensing technologies and performance grades,” 06 2023.
- [11] I. Aerosmith, “2103c series three axis position and rate table system.” <https://www.ideal-aerosmith.com/wp-content/uploads/2024/02/2102C.pdf>. Accessed: March 30, 2025.
- [12] H. Rahimi and A. A. Nikkhah, “Improving the calibration process of inertial measurement unit for marine applications,” *NAVIGATION: Journal of the Institute of Navigation*, vol. 67, no. 4, pp. 763–774, 2020.
- [13] A. Kozlov and F. Kapralov, “Millimeter-level calibration of imu size effect and its compensation in navigation grade systems,” in *2019 DGON Inertial Sensors and Systems (ISS)*, pp. 1–12, 2019.
- [14] X. Li, W. Huang, X. Zhu, and Z. Zhao, “Mems-imu error modelling and compensation by 3d turntable with temperature chamber,” in *2022 International Symposium on Networks, Computers and Communications (ISNCC)*, pp. 1–5, 2022.
- [15] C.-Y. Hung and S.-C. Lee, “A calibration method for six-accelerometer ins,” *International Journal of Control Automation and Systems*, vol. 4, 10 2006.

- [16] Q. Cai, G. Yang, N. Song, and Y. Liu, “Systematic calibration for ultra-high accuracy inertial measurement units,” *Sensors*, vol. 16, no. 6, 2016.
- [17] Safran, “Stim300 imu non-gps aided inertial measurement unit.” <https://safran-navigation-timing.com/product/stim300/>. Accessed: March 30, 2025.

6 Appendix

6.1 Traditional IMU Calibration Post-Processing

From equation 2 and collected test data listed in table 1, the accelerometer bias \mathbf{b}_a can be solved from the collected test data.

$$\mathbf{b}_a = \begin{bmatrix} b_{a,x} \\ b_{a,y} \\ b_{a,z} \end{bmatrix} = \frac{1}{2} \begin{bmatrix} \bar{f}_x^{+x} + \bar{f}_x^{-x} \\ \bar{f}_y^{+y} + \bar{f}_y^{-y} \\ \bar{f}_z^{+z} + \bar{f}_z^{-z} \end{bmatrix} \quad (18)$$

Likewise, accelerometer scale factor terms within the quantity M_a can also be computed, where g is the magnitude of the accelerometer due to gravity at that specific location at the inertial test laboratory.

$$\mathbf{s}_a = \begin{bmatrix} s_{a,x} \\ s_{a,y} \\ s_{a,z} \end{bmatrix} = \frac{1}{2g} \begin{bmatrix} \bar{f}_x^{+x} - \bar{f}_x^{-x} \\ \bar{f}_y^{+y} - \bar{f}_y^{-y} \\ \bar{f}_z^{+z} - \bar{f}_z^{-z} \end{bmatrix} - 1 \quad (19)$$

Accelerometer misalignment uses off-axis terms from each collected test where each misalignment term is computed separately.

$$\begin{aligned} m_{a,xy} &= \frac{1}{2g} (\bar{f}_x^{+y} - \bar{f}_x^{-y}) \\ m_{a,xz} &= \frac{1}{2g} (\bar{f}_x^{+z} - \bar{f}_x^{-z}) \\ m_{a,yx} &= \frac{1}{2g} (\bar{f}_y^{+x} - \bar{f}_y^{-x}) \\ m_{a,yz} &= \frac{1}{2g} (\bar{f}_y^{+z} - \bar{f}_y^{-z}) \\ m_{a,zx} &= \frac{1}{2g} (\bar{f}_z^{+x} - \bar{f}_z^{-x}) \\ m_{a,zy} &= \frac{1}{2g} (\bar{f}_z^{+y} - \bar{f}_z^{-y}) \end{aligned} \quad (20)$$

Also from equation 2, the gyroscope bias \mathbf{b}_g can be solved from the collected test data.

$$\mathbf{b}_g = \begin{bmatrix} b_{a,x} \\ b_{a,y} \\ b_{a,z} \end{bmatrix} = \frac{1}{2} \begin{bmatrix} \bar{\omega}_x^{+x} + \bar{\omega}_x^{-x} \\ \bar{\omega}_y^{+y} + \bar{\omega}_y^{-y} \\ \bar{\omega}_z^{+z} + \bar{\omega}_z^{-z} \end{bmatrix} \quad (21)$$

Gyroscope scale factor terms within the quantity M_g can also be computed, where ω_{test} is the magnitude of the accelerometer due to gravity at that specific location at the inertial test laboratory.

$$\mathbf{s}_g = \begin{bmatrix} s_{g,x} \\ s_{g,y} \\ s_{g,z} \end{bmatrix} = \frac{1}{2\omega_{\text{test}}} \begin{bmatrix} \bar{\omega}_x^{+x} - \bar{\omega}_x^{-x} \\ \bar{\omega}_y^{+y} - \bar{\omega}_y^{-y} \\ \bar{\omega}_z^{+z} - \bar{\omega}_z^{-z} \end{bmatrix} - 1 \quad (22)$$

Gyroscope misalignment uses off-axis terms from each collected test where each misalignment term is computed separately.

$$\begin{aligned} m_{g,xy} &= \frac{1}{2\omega_{\text{test}}} (\bar{\omega}_x^{+y} - \bar{\omega}_x^{-y}) \\ m_{g,xz} &= \frac{1}{2\omega_{\text{test}}} (\bar{\omega}_x^{+z} - \bar{\omega}_x^{-z}) \\ m_{g,yx} &= \frac{1}{2\omega_{\text{test}}} (\bar{\omega}_y^{+x} - \bar{\omega}_y^{-x}) \\ m_{g,yz} &= \frac{1}{2\omega_{\text{test}}} (\bar{\omega}_y^{+z} - \bar{\omega}_y^{-z}) \\ m_{g,zx} &= \frac{1}{2\omega_{\text{test}}} (\bar{\omega}_z^{+x} - \bar{\omega}_z^{-x}) \\ m_{g,zy} &= \frac{1}{2\omega_{\text{test}}} (\bar{\omega}_z^{+y} - \bar{\omega}_z^{-y}) \end{aligned} \quad (23)$$